

# The Interpretation of Phase and Intensity Data from AMCW Light Detection Sensors for Reliable Ranging

M. D.Adams\* P. J.Probert  
Department of Engineering Science  
University of Oxford  
Oxford, United Kingdom

## Abstract

*The analysis of sensor range data and its application to mobile robot navigation are of crucial importance in the field of mobile robotic research.*

*We analyze the range data produced by an amplitude-modulated continuous wave (AMCW) light detection and ranging sensor and show that by physically modeling such sensors, we not only can produce reliable range estimates, but can also quantify our certainty in each range data point. We discuss the noise in the sensor and show the importance of using both phase and intensity data for calibration and data interpretation.*

*We consider in detail the phenomenon of “mixed pixel points” whereby false range measurements occur when the light beam transmitted is split between two or more surfaces of differing range and/or reflectivity. We describe a new algorithm capable of detecting sudden changes in surface reflectance and/or range in order to identify these “spurious” data points. We quantify the regions over which the detection method will work, as we consider its sensitivity to changes in range and surface reflectance, while also quantifying the possibility of falsely predicting a discontinuity.*

## 1 Introduction

In the field of mobile robotics, range sensing is a crucial component of any autonomous system. Mobile robot navigation using simple planar depth maps produced from ranging sensors is still in its infancy. Manipulating the range data robustly in the presence of range uncertainty is still a problem, even with simple sensors, as will be demonstrated in this article.

The type of sensor considered here is a time-of-flight range finder that greatly reduces the correspondence problems associated with stereo vision and removes the disparity problem associated with triangulation systems by keeping the transmitted and received beams coaxial. This type of sensor consists of a transmitter that illuminates a target with a collimated beam and a receiver capable of detecting the component of light which is essentially coaxial with the transmitted beam. Often referred to as *optical radars* or *lidars* (light detection and ranging), these devices produce a range estimate from the time needed for the light to reach the target and return. A mechanical mechanism sweeps the light beam to cover the required scene.

It is possible to determine the time of flight of the light beam using a pulsed laser, thus measuring the elapsed time directly (Johnston A. R. 73). Electronics capable of resolution in picoseconds are required in such devices, and the devices are therefore often very expensive. A second method is to measure the beat frequency between a *frequency-modulated continuous wave* (FMCW) and its reflection. A survey of such devices and their application to obstacle

---

\*M. D.Adams is now at the Swiss Federal Institute of Technology, Zürich, Switzerland.

surface reconstruction is covered in (Besl P. J. 88). For close-range applications, a simple means of determining the time of flight of the light is by measuring the phase shift between an *amplitude-modulated continuous wave* (AMCW) and its received reflection. Measuring phase shift to produce range estimation is technically easier than the above two methods. This is shown by the fact that AMCW range finders are beginning to become commercially available (Cox I. J. 88; Hebert M. et al. 89; Krotkov E. 90).

The purpose of this article is to develop a model of an AMCW optical radar in such a way that we can use the data to guide a mobile vehicle locally. We scan the environment with a rotating plane mirror so that a two-dimensional planar depth map of a mobile’s surroundings is created. While it is true that humans perceive their surroundings by both vertical and horizontal scanning, the amount of information in scanning in a horizontal plane in itself can be sufficient for path planning in an indoor office/laboratory-type environment. We therefore restrict our research to horizontal scanning scene analysis only.

In Section 2 we will explain the range estimation technique employed in an AMCW optical range finder. Knowledge of this method is essential when modeling sensor defects.

In Section 3 the sources of noise in the electronic signal produced by the photo diode are explored. The propagation of these noise sources through the sensor to the range estimate is also considered. We then derive a relationship between the expected range variance and the detected signal amplitude.

Section 4 shows some initial results from the AMCW infrared sensor and also shows some of the problems associated with the particular sensor used. In Section 4.3 we note another defect of the AMCW ranging technique, caused by sudden changes in range and/or surface reflectance. While this effect has been observed in previous literature (Hebert M. and Krotkov E. 91; Hinkel R. and Weidmann M. 89), no efforts have been made to solve the problem. Our measurements demonstrate that even in an optical sensor, the finite width of the light beam can be a significant problem.

In Section 5 we consider, in detail, the effect of splitting the light beam between surfaces of differing ranges and reflectivity. Section 5.1 describes the applications of the sensor as a discontinuity detector capable of detecting sudden changes in surface reflectance and/or range in order to identify “spurious” data points (often referred to as mixed pixel points [(Hebert M. and Krotkov E. 91; Nitzan D. et al. 77)]). We quantify the regions over which the detection method will work as we consider its sensitivity to changes in range and surface reflectance, while also quantifying the possibility of falsely predicting a discontinuity.

The particular sensor used was developed at AT&T Bell Laboratories in the United States. Section 5.5 demonstrates the discontinuity detector using data from the sensor.

## 2 Infrared Phase Estimation

Near infrared light (from a light-emitting diode [LED]) is collimated and transmitted from the transmitter  $\mathbf{T}$  in Figure 1 and hits a point  $\mathbf{P}$  in the environment. For surfaces having a roughness greater than the wavelength of the incident light, diffuse reflection will occur, meaning that the light is reflected almost isotropically. The wavelength of the infrared light emitted is 824 nm, meaning that most surfaces, with the exception of only highly polished reflecting objects, will be diffuse reflectors. The component of the infrared light that falls within the receiving aperture of the sensor will, for distant objects, return almost parallel to the transmitted beam.

The sensor transmits 85% amplitude modulated light at a known frequency and measures the phase shift between the transmitted and reflected signals. The wavelength of the modulating signal obeys the equation:

$$c = f\lambda \tag{1}$$

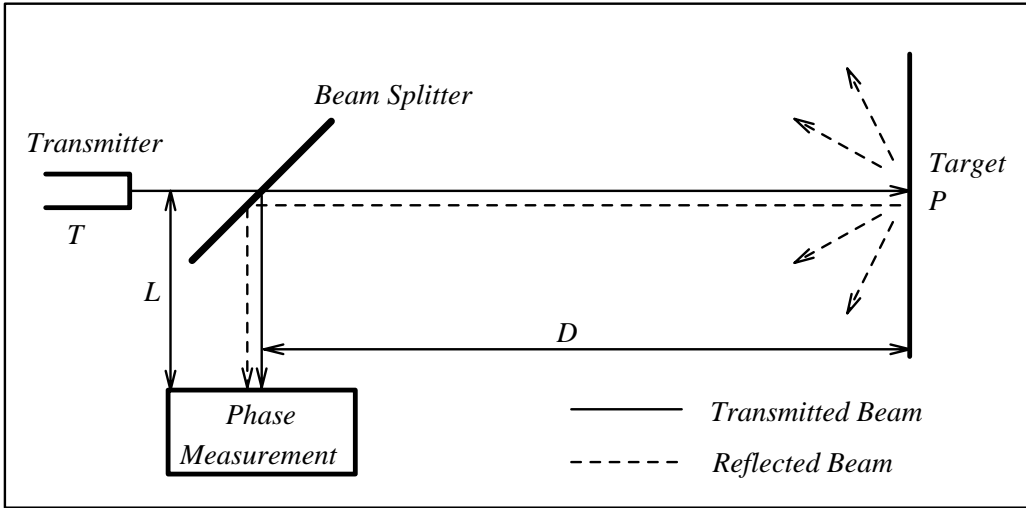


Figure 1: *Infrared light sensing by modulated signal transmission. The transmitted beam is split so that most of it illuminates the target and a small part of it reaches the phase sensor, to act as a reference signal.*

where  $c$  is the speed of infrared light and  $f$  the modulating frequency. For  $f = 5$  MHz (as in the AT&T sensor),  $\lambda = 60$  m. The total distance covered by the emitted light is  $D'$ , where:

$$D' = L + 2D = L + \frac{\theta}{2\pi}\lambda, \quad (2)$$

where  $D$  and  $L$  are the distances defined in Figure 1. The required distance  $D$ , between the beam splitter and the target, is therefore given by:

$$D = \frac{\lambda}{4\pi}\theta, \quad (3)$$

$\theta$  is the electronically measured phase difference between the transmitted and reflected light beams, and  $\lambda$  the known modulating wavelength. It can be seen that the transmission of a single amplitude-modulated wave can theoretically result in ambiguous range estimates, since for  $\lambda = 60$  m, a target at a range of 5 m would give an indistinguishable phase measurement from a target at 20 m, since each phase angle would be  $180^\circ$  apart.<sup>1</sup> We therefore define an “ambiguity interval” of  $\lambda/2$ , but in practice we note that the range of the sensor is much lower than  $\lambda/2$  due to the attenuation of infrared light in air.

### 3 Noise Propagation Within the Sensor

In reality the phase estimate produced by such a sensor becomes more useful when it is combined with the *amplitude* or strength of the returned light signal. The returned light incident on the sensor’s receiving photodiode is the result of the emission of photons from the illuminated target. The “mean value effect” of this emission produces a signal having the form of the transmitted modulated carrier, but the overall effect is known to be approximately governed by a Poisson process (Nitzan D. et al. 77).

<sup>1</sup>This depends on the phase discriminator used. A simple exclusive OR gate (as used in our sensor) can only measure phase differences up to  $180^\circ$  apart, but more elaborate phase measuring techniques can measure phase differences up to  $360^\circ$  without ambiguity.

The photodiode acts as a current source that produces a time-varying current at the frequency of the modulating signal. However, in a diode the emission of electrons from the cathode that produces the current has random properties that gives rise to a mean square *shot noise* current (Connor F. R. 82). This means that the *voltage* waveform produced electronically from the photodiode current, is made up of two components. First, the signal voltage  $V_p$  given by

$$V_p = V_r \cos(\omega t + \phi), \quad (4)$$

where the amplitude  $V_r$  is proportional to the amplitude of the modulating wave,  $\phi$  is the modulation phase relative to the transmitted wave, and  $\omega$  is the angular frequency of the modulating signal. Superimposed on this signal we have an electronic noise voltage  $\bar{V}_n$ , having a variance  $\langle \sigma_n^2 \rangle$ . This noise term is made up primarily of shot noise from the photodiode and thermal noise from the resistors used in the electronic circuits.<sup>2</sup>

At the phase comparator the range is estimated from the phase difference shown in Figure 2. The relationship between the standard deviation in the absolute *phase* of the received signal  $\sigma_\phi$

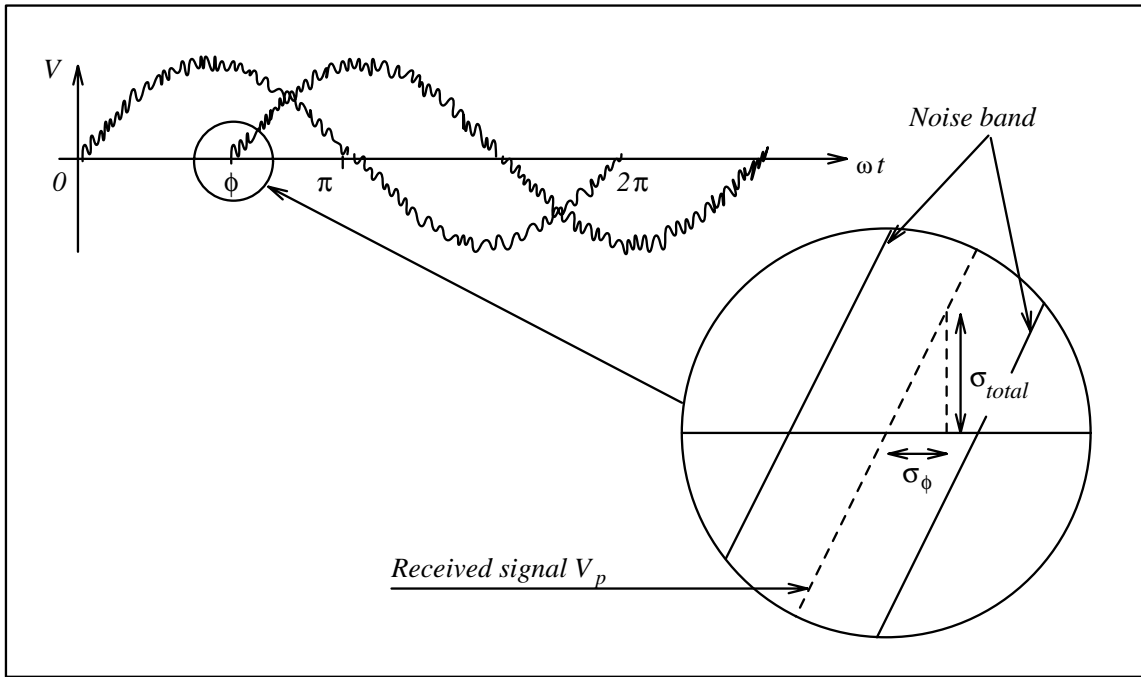


Figure 2: *Phase estimation in the presence of noise. The finite width of the sinusoidal waves demonstrates the method of electrical noise propagation through to the range estimate at the sensor output.*

to the combined electronic and photon noise standard deviation  $\sigma_{total}$  received by the receiver electronics can be seen graphically as a *noise triangle* (Miller G. L. and Wagner E. R. 87) which, from Figure 2, gives

$$\frac{\sigma_{total}}{\sigma_\phi} = \left| \frac{\partial V_p}{\partial(\omega t)} \right|_{V_p=0} \quad (5)$$

where  $\left| \frac{\partial V_p}{\partial(\omega t)} \right|_{V_p=0}$  is the magnitude of the change of received signal voltage with phase at the zero crossing (i.e. when the wave cuts the  $\omega t$  axis). From equations (4) and (5), (Adams M. D.

<sup>2</sup>Photon noise also contributes to the total noise voltage. A more exact analysis that takes this into account is given in (Adams M. D. 92).

92) shows that an approximate relationship between the range variance  $\langle \sigma_r^2 \rangle$  and the received signal amplitude  $V_r$  is given by

$$\langle \sigma_r^2 \rangle \approx \langle \sigma_n^2 \rangle \left( \frac{\lambda}{4\pi} \right)^2 \left( \frac{1}{V_r} \right)^2 + \langle \sigma_e^2 \rangle, \quad (6)$$

where  $\lambda$  is the modulation wavelength,  $\langle \sigma_n^2 \rangle$  is the total electronic noise variance, and  $\langle \sigma_e^2 \rangle$  is the variance of any noise sources introduced *after* phase comparison.

The relationship derived in equation (6) will be used in Section 4 to establish the experimental values of  $\langle \sigma_n^2 \rangle$  and  $\langle \sigma_e^2 \rangle$  and, hence, the numerical relationship between  $\langle \sigma_r^2 \rangle$  and  $V_r$ .

## 4 Calibrating the Sensor: Results

To be able to quantify the certainty of each range reading produced by the sensor, we need to determine the parameters in equation (6). To find these parameters, simple experiments were done in which a thousand independent range measurements were made of a fixed target with the sensor stationary.

The histograms in Figure 3 have horizontal axes showing the measured range  $r$ , produced from the sensor's phase estimate and vertical axes showing the number of readings that have a particular range reading  $r$ . Note that the curves show distributions that are normalized, since

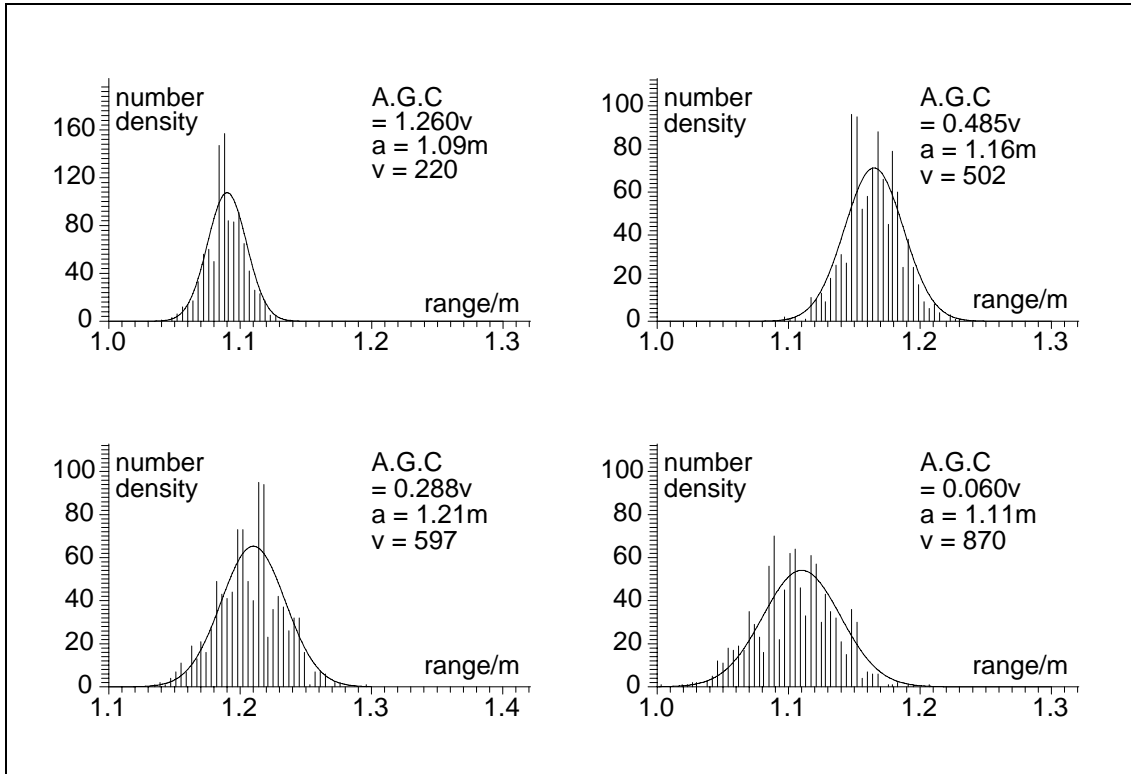


Figure 3: *Histograms showing the effect of different coloured targets at a given range. All targets were at a range of 1.17 m from the sensor, but were changed from white to orange, orange to green and green to grey running from the top left graph to the bottom right graph respectively. The signal strength values (marked as ‘A.G.C’), sample means  $a$  and sample variances  $v \times 10^{-6} \text{ m}^2$  are shown with each graph. The continuous curves show calculated Gaussian distributions with the same mean and variance as the discrete data.*

the sum of the heights of all the range measurements is constant (one thousand in our case). All of the histograms in Figure 3 were produced from different targets at a fixed range (1.17 m) from the sensor. Each histogram is labeled with the received signal strength, the sample mean  $\bar{r}$ , and the sample variance  $\langle \sigma_r^2 \rangle$ , found by entering all 1000 data points into the equations:

$$\bar{r} = \frac{1}{n} \sum_{i=1}^n r_i, \quad \langle \sigma_r^2 \rangle = \frac{1}{n} \sum_{i=1}^n (r_i - \bar{r})^2, \quad n = 1000 \quad (7)$$

Hence, as expected, different signal strength values correspond to different variances within the range values and the histograms show that as the returned signal strength decreases, the range measurements have a greater spread as the variance increases. Note that the distributions are approximately Gaussian. Figure 3 also shows the significant changes in the sample mean of the ranges for different signal strengths. These large shifts in the sample means are simply modeled as systematic errors to be accounted for when modeling the sensor.

#### 4.1 Range Variance: Calibration

Equation (6) in Section 3 suggested an inverse square relationship between  $\langle \sigma_r^2 \rangle$  and  $V_r^2$ . We applied a least squares inverse square function fit using only data (recorded to produce the histograms of Figure 3) with  $(1/V_r)^2 < 15$  (volts)<sup>-2</sup>, since the rest of the data will corrupt the least squares fit.<sup>3</sup>

The top graph in Figure 4 shows the resulting function with the used data. The function (shown as a continuous line in Figure 4) that matches the data in the least squares sense is:

$$\langle \sigma_r^2 \rangle \approx \frac{106.301}{V_r^2} + 169.541, \quad (8)$$

where  $V_r$  is measured in volts and  $\sigma_r^2$  is the variance  $\times 10^{-6}$  m<sup>2</sup>. By direct comparison with equation (6) we see that for  $\lambda = 60$  m:

$$\langle \sigma_n^2 \rangle \approx 4.663 \times 10^{-6} \text{ (volts)}^2, \quad \langle \sigma_e^2 \rangle = 169.541 \times 10^{-6} \text{ (m)}^2 \quad (9)$$

Therefore, for each observed range estimate, we now have an approximate estimate of the range variance.

The bottom curve in Figure 4 shows the electronic systematic phase errors as a function of the returned amplitude. The two curves provide a complete calibration of the sensor.

#### 4.2 Range Measurement: Results

We are now able to use the sensor data (returned signal strength and range estimate) to the full. Figure 5 shows a 360° scan taken in Oxford's AGV laboratory, using all eight bits of the range analogue to digital converter to focus on ranges between 0.0 and 2.5 m only. The left scan in Figure 5 shows the scan result following calibration using the lower graph in Figure 4.

With the top calibration curve of Figure 4 it is also possible to estimate the uncertainty in each range estimate. The right plot in Figure 5 shows the same scan result except that it also shows lines, centered on the corrected range observations, of length  $2\sigma_r$  (i.e. twice the standard

---

<sup>3</sup>This is because the range variance cannot increase without limit, since the phase measurement of an AMCW range finder is defined modulo  $2\pi$  only. Therefore, the range is defined modulo  $\lambda/2$ , which is the ambiguity interval discussed in Section 2. When  $V_r \rightarrow 0$ , the range distribution tends toward a rectangle between ranges of 0 and  $\lambda/2$  m and a height of  $2000/\lambda$  (giving our normalized distribution of 1000 range readings). The range variance therefore tends toward the second moment of the area of this rectangular range distribution.

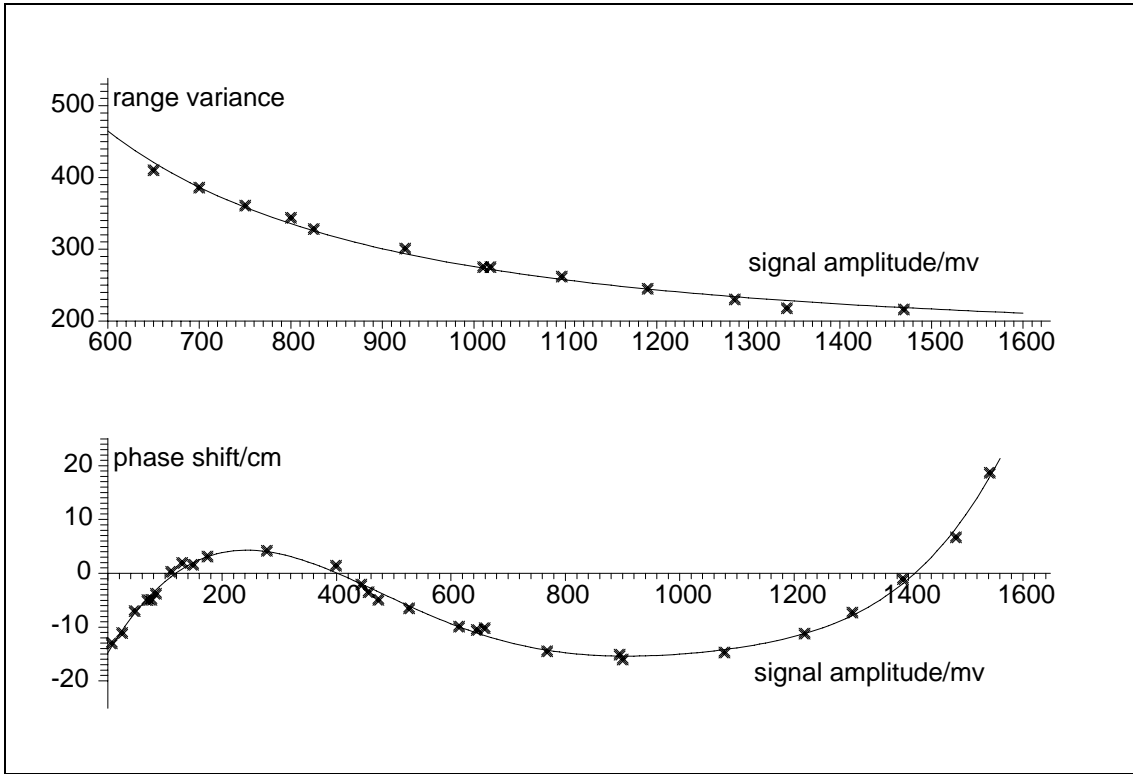


Figure 4: *Least squares function fits to the experimental data (shown as crosses) of range variance  $\times 10^{-6}$  (top curve) and phase shift (bottom curve) versus signal strength.*

deviation associated with the returned signal strength from equation (8)) in order to show the certainty. We can see that the standard deviation associated with the spurious points (points that do not correspond to any point within the environment) E and F is extremely large due to low signal amplitude from these data points.

### 4.3 Other Sensor Defects

Close examination of Figure 5 shows that spurious data points sometimes result immediately before or after detected edges and surface reflectance changes. Between regions D and F in Figure 5 for example, the actual range suddenly jumps from 1.26 m (corresponding to the edge at D on surface AD) to 2.50 m (the first detected range on surface FG, the maximum range of the sensor in this case). The observed range, according to the sensor, changes from 1.26 m to only 1.61 m (point E in Figure 5).

To quantify this effect, we consider in the next section the problem of receiving two amplitude-modulated signals, one from each illuminated surface.

## 5 Simultaneous Reflection of Signals From Two Surfaces

In order to identify spurious data points, the effects of simultaneous reflection from two targets warrant further investigation. In (Hebert M. and Krotkov E. 91), an AMCW lidar is used to form two-dimensional pixel images. In this work the above effect is noted and referred to as the phenomenon of *mixed pixels*. It is stated that it is a problem inherent to direct detection AMCW laser radars and that it cannot be completely eliminated with such sensors. One approach to

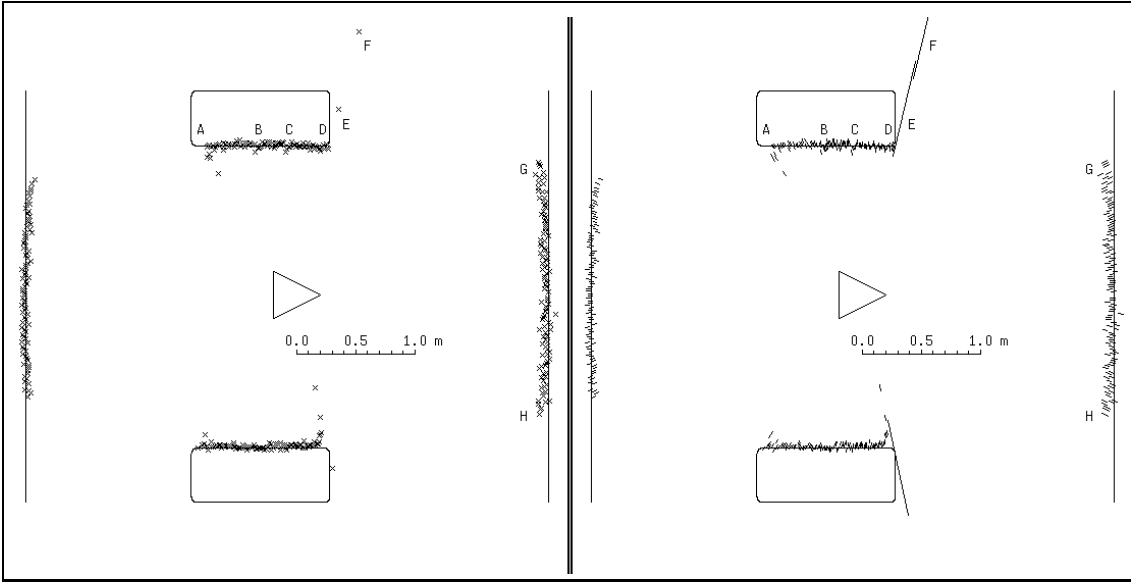


Figure 5: *The sensor is positioned at the center of the triangle shown. In the left hand plot the data has been corrected according to the lower calibration curve above. In the right hand scan, lines are centered on the corrected range observations having lengths equal to twice the standard deviation associated with the returned signal strength.*

the problem offered in (Hebert M. and Krotkov E. 91) is the application of a median filter to the scan which orders a batch of range data in values of increasing range and selects the median value (i.e. this method has the effect of removing “outliers” from a batch of data). In our case the median value that would then be selected to represent the data could well be the spurious point we are trying to remove. (Adams M. D. 92) shows that in this respect the median filter can fail catastrophically. An alternative approach would be to examine the change in range with respect to sensor angle or time. This technique can, under certain conditions, offer a solution to identifying such points, but is not fool-proof since certain environmental orientations can provide large range gradients with respect to sensor angle or time. Before considering any particular method for identifying these points, we will analyze the physics involved when an infrared beam is split between two surfaces.

Consider a transmitted reference signal  $V_0 \cos \omega t$  that is incident on an edge (Figure 6). An area  $A_1$  is illuminated on the closer of the two surfaces returning a signal  $V_1 \cos(\omega t + \phi_1)$ , while an area  $A_2$  is illuminated on the further surface, yielding a signal  $V_2 \cos(\omega t + \phi_2)$ . The signal returned to the sensor will actually be the result of many modulated signals  $\sum_{i=1}^n V_i \cos(\omega t + \phi_i)$ , each being emitted from a small area  $\delta A_i$  within the infrared beam cross section. For a small beam cross-sectional area, the analysis is simplified if we assume that during the time the beam traverses the edge,  $\phi_1$  and  $\phi_2$  remain constant and  $V_1$  and  $V_2$  change only with changes in  $A_1$  and  $A_2$ . Changes in  $\phi$  as the beam moves across areas  $A_1$  or  $A_2$  individually are therefore assumed to be negligible. Hence the returned signal  $Y$  is given by

$$Y = V_1 \cos(\omega t + \phi_1) + V_2 \cos(\omega t + \phi_2), \quad (10)$$

so that

$$Y = [V_1 \cos \phi_1 + V_2 \cos \phi_2] \cos \omega t - [V_1 \sin \phi_1 + V_2 \sin \phi_2] \sin \omega t, \quad (11)$$

which can be written as a single sinusoid:

$$Y = V \cos \phi \cos \omega t - V \sin \phi \sin \omega t = V \cos(\omega t + \phi), \quad (12)$$

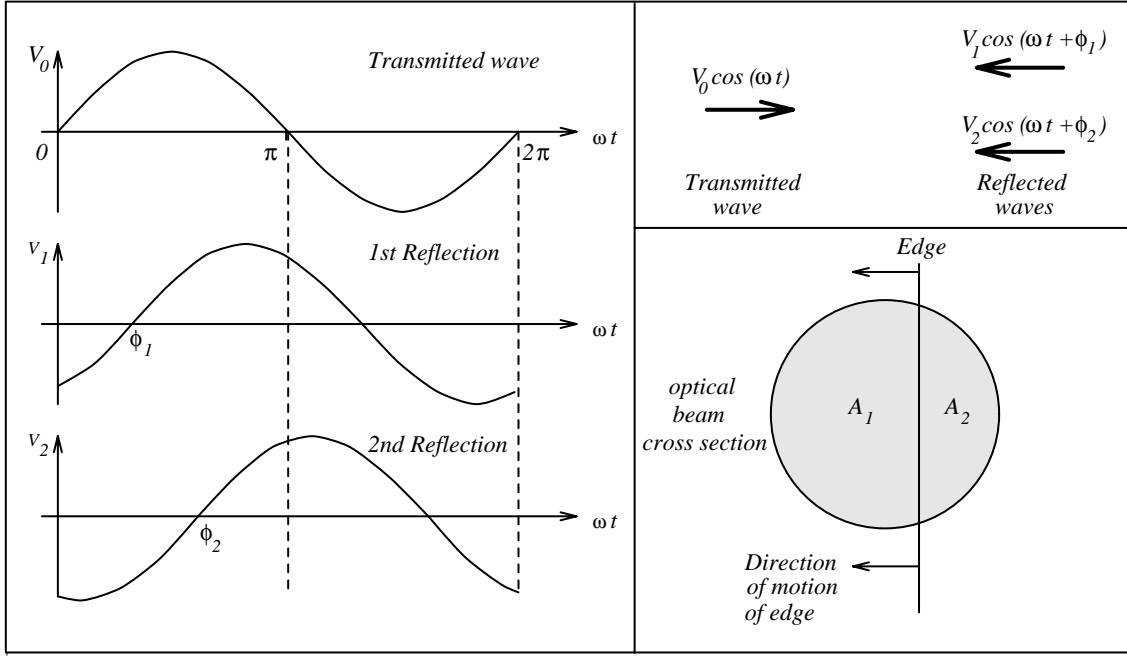


Figure 6: The transmitted signal is split into two returned signals of differing phase by an edge. As the beam traverses the edge the illuminated areas and hence returned signal amplitudes will vary with traversal time.

which is the form that is estimated at the sensor outputs (i.e.  $V$  is the output signal strength produced by both targets and  $\phi$  the resulting phase shift).

To quantify the “spurious point” effect, we need to find  $V$  and  $\phi$  as functions of time, as the beam crosses the edge. From equations (11) and (12) we see that

$$\cos \phi = \frac{V_1}{V} \cos \phi_1 + \frac{V_2}{V} \cos \phi_2 \quad (13)$$

and

$$\sin \phi = \frac{V_1}{V} \sin \phi_1 + \frac{V_2}{V} \sin \phi_2, \quad (14)$$

giving two simultaneous equations in  $V$  and  $\phi$ . Eliminating  $\phi$  gives

$$V^2 = V_1^2 + 2V_1V_2 \cos(\phi_1 - \phi_2) + V_2^2. \quad (15)$$

Before we can proceed further, we need to determine, as generally as possible, the relationship between each returned voltage, the sensor-to-target range and the illuminated area. We make the assumption that the emitted power is uniformly distributed over the cross-sectional area of the beam. Therefore

$$V_{1,2} = K_{1,2} \frac{A_{1,2}}{F(R_{1,2})}, \quad (16)$$

where the subscripts 1 and 2 refer the reflected signals 1 and 2,  $K_{1,2}$  are constants for each surface and incorporate surface reflectances and beam-to-target angles of incidence, and  $F(R_{1,2})$  represents a function of the sensor to target ranges  $R_{1,2}$ .

To establish a relationship between  $K_1$  and  $K_2$  in equations (16), we consider the magnitude of the returned signal strengths when each surface is illuminated *independently*. We denote these as  $V_{e1}$  and  $V_{e2}$ . We will call these the *end* conditions and in general

$$V_{e2} = \eta V_{e1}, \quad \frac{K_1}{K_2} = \frac{V_{e1} F(R_1)}{V_{e2} F(R_2)}. \quad (17)$$

Hence, by substituting of equations (16) and (17) into equation (15) we get

$$V^2 = \frac{K_1^2}{[F(R_1)]^2} [A_1^2 + 2\eta A_1 A_2 \cos(\phi_1 - \phi_2) + \eta^2 A_2^2]. \quad (18)$$

When the beam is equally divided between the two surfaces,  $A_1 = A_2 = (\pi b^2/2)$ , where  $b$  is the optical beam radius, we see that

$$V = \frac{K_1 b^2 \pi}{2F(R_1)} [(1 + \eta^2) + 2\eta \cos(\phi_1 - \phi_2)]^{1/2}, \quad (19)$$

which is the returned signal amplitude. Substitution into equation (13) then yields

$$\cos \phi = \frac{\cos \phi_1 + \eta \cos \phi_2}{[(1 + \eta^2) + 2\eta \cos(\phi_1 - \phi_2)]^{1/2}}. \quad (20)$$

For the particular case when  $\eta = 1$  (i.e. when each surface individually returns the same signal strength)

$$V = \frac{K_1 b^2 \pi}{F(R_1)} \cos\left(\frac{\phi_1 - \phi_2}{2}\right), \quad (21)$$

and the phase is simply averaged:

$$\phi = \frac{\phi_1 + \phi_2}{2}. \quad (22)$$

The above theory can be used for the detection of range readings such as points E and F in Figure 5. We will show in the following section that the motion of the infrared beam across an edge is only a particular case to which the above theory can be applied. The estimated phase and amplitude of any single reading can be considered to be the result of the addition of two signals from any two arbitrary “end” conditions, that do not have to lie either side of an edge. By generalizing this theory to any range and amplitude estimate, we will derive a method for the detection of spurious data such as points E and F in Figure 5 and, just as importantly, we will quantify the possibility of false detection. By “false detection” we mean the false labelling of a correct data point as spurious.

Close examination of Figure 5 reveals that some of the spurious points (such as those at E and F in the Figure) lie *closer* than the true discontinuity and not *between* the true range readings as predicted by the preceding theory. This is the result of an electronic problem with the particular sensor used and occurs due to direct cross-talk between the high-frequency transmitter circuit and the receiver. At a discontinuity, the amplitude measurements are very low, and any small amount of cross-talk directly between the transmitter and the receiver will distort the measured phase and, hence, the range estimate produced by the sensor.

## 5.1 Discontinuity Detection: The Physics

Before proceeding, we make a distinction between what we will refer to as a *discontinuity* and an *edge*. We will use the term discontinuity to refer to an abrupt change in the signal amplitude. We label an edge as an abrupt change in the sensor-to-target range (i.e. a real change in range in the world recorded by the sensor), as humans would perceive a true edge. Note that a discontinuity is a change in the sensor’s output amplitude signal and can be the result of an edge *and/or* a change in surface reflectance, as the sensor head rotates.

We also now clarify the constraints on our end conditions. Equation (18) is valid only if the sum of the components of the areas normal to the optical beam, that illuminates each end point, is constant; i.e.

$$A_1 + A_2 = A, \quad (23)$$

where  $A$  is the cross-sectional area of the beam. This means that the chosen end conditions must be spatially joined in the plane of the scanning infrared beam. This is shown in Figure 7. We assume that there is a vertical boundary across which there is a possible change in range or

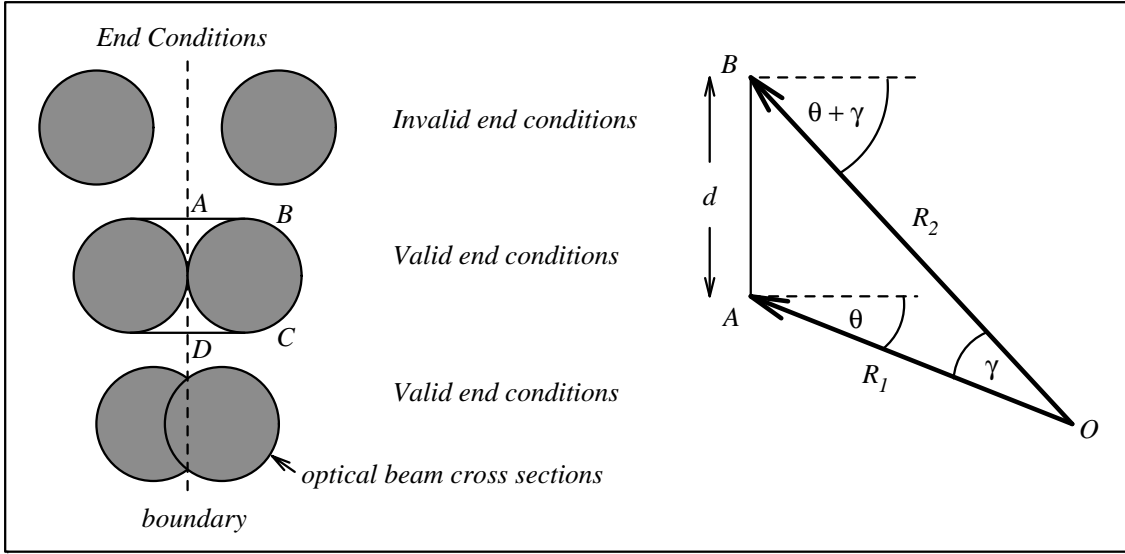


Figure 7: *The relationship between chosen end conditions.*

surface reflectance. Due to the small optical beam diameter (2 cm in our case), we make the approximation that an “end condition” is not just restricted to the circular beam cross section, but occupies the arched region marked ABCD in Figure 7. This means that equation (23) is valid in equation (18). Within the arched region ABCD, the *actual* values of  $R_1$  and  $K_1$  can change, but the *sensed* values of  $R_1$  and  $K_1$  will remain constant.

Eliminating  $A_2$  in equation (18) from equation (23), and differentiating  $V^2$  with respect to variable  $A_1$  shows that there is always a position between the end points at which  $V$  is stationary with respect to  $A_1$ . The second derivative of the square of the signal amplitude with respect to  $A_1$  is given by:

$$\frac{\partial^2(V^2)}{\partial A_1^2} = \frac{2K_1^2}{F(R_1)^2} [1 + \eta^2 - 2\eta \cos(\phi_1 - \phi_2)] \quad (24)$$

which is independent of  $A_1$ .  $\partial^2(V^2)/\partial A_1^2$  is therefore constant as the beam traverses from one end condition to the other, the value of this constant being dependent on the end conditions only (i.e.  $\phi_1$ ,  $\phi_2$ ,  $\eta$  and  $K_1$ ). From equation (24) we can find the nature of the stationary value of  $V^2$  versus  $A_1$ . Simple analysis shows that for all values of  $\phi_1$ ,  $\phi_2$  and  $\eta$ ,  $\partial^2(V^2)/\partial A_1^2$  is always positive (meaning that  $V^2$  has a minimum with respect to  $A_1$ ) and approaches zero as  $\eta \rightarrow 1$  and  $\phi_1 \rightarrow \phi_2$  (i.e. if the end conditions are similar,  $\partial^2(V^2)/\partial A_1^2 \rightarrow 0$ ). This is demonstrated by the experimental results shown in Figure 8 where  $V$  is plotted against time. We can therefore conclude that the numerical value of  $\partial^2(V^2)/\partial A_1^2$  across two end conditions gives us an indication of how “different”, in terms of either sensor-to-target range and/or surface reflectance, the end conditions are.  $\partial^2(V^2)/\partial A_1^2$  will rarely actually be zero in practice, since two end conditions will rarely be identical, even when the beam does not pass a discontinuity. It therefore remains for us to determine a value for  $\partial^2(V^2)/\partial A_1^2$ , beyond which we assume a discontinuity has been passed, possibly resulting in spurious data such as E and F in Figure 5.

We also need to note that the reflected infrared light from a target contains two components, one being a specular component that follows Fresnel’s equations and the other a diffuse component that is approximately described by Lambert’s cosine law (Moon P. 61). Because of

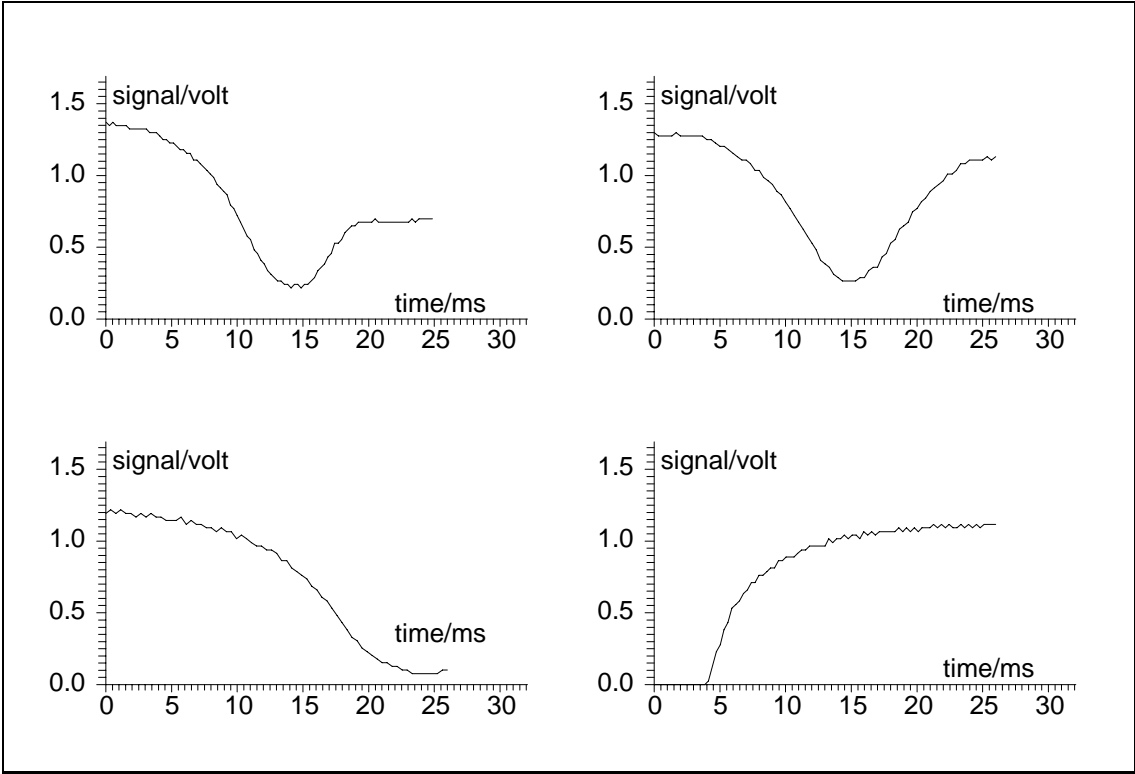


Figure 8: *Graphs of signal amplitude versus time as the infrared beam traverses different end conditions.*

the coaxial design of the sensor, specular reflections can be received only at very near normal incidence and in practice are noticed only with extremely reflective targets. Therefore, except for these rather rare cases, only the diffuse component need be considered.

We now consider in more detail the value of  $\partial^2(V^2)/\partial A_1^2$  when the beam traverses a discontinuity. Consider the right hand diagram in Figure 7.  $R_1$  and  $R_2$  are two successive range estimates that we will choose as arbitrary end conditions. According to Lambert's cosine law, the amplitude of the returned signal in each case is given by

$$V_{e1} = \frac{\rho_1 A \cos \theta}{R_1^2}, \quad V_{e2} = \frac{\rho_2 A \cos(\theta + \gamma)}{R_2^2}, \quad (25)$$

where  $\rho_{1,2}$  are the surface reflectance constants from points A and B and  $\gamma$  is the angle between resulting data points. In general, between end points A and B in Figure 7,  $\rho_1 \neq \rho_2$ . Hence, from the figure

$$\eta = \frac{V_{e2}}{V_{e1}} = \frac{\rho_2 R_1^2 \cos(\theta + \gamma)}{\rho_1 R_2^2 \cos \theta} = \frac{\rho_2}{\rho_1} \left( \frac{R_1}{R_2} \right)^3 \quad (26)$$

Applying the sine rule to triangle OAB in Figure 7 and from equations (25) and (26) we define  $S$  as

$$S = \frac{\partial^2(V^2)}{\partial A_1^2} = 2\rho_1^2 \frac{R_2^2 \sin^2 \gamma}{d^2 R_1^4} \left[ 1 + \left( \frac{\rho_2}{\rho_1} \right)^2 \left( \frac{R_1}{R_2} \right)^6 - 2 \left( \frac{\rho_2}{\rho_1} \right) \left( \frac{R_1}{R_2} \right)^3 \cos[K(R_1 - R_2)] \right] \quad (27)$$

where  $K$  is a constant relating phase shift to actual range and  $R_1$  and  $R_2$  are related by the cosine rule:

$$d^2 = R_1^2 + R_2^2 - 2R_1 R_2 \cos \gamma. \quad (28)$$

Between equations (27) and (28), it is possible to eliminate  $d$  and determine a relationship between  $S$ ,  $R_1$ ,  $R_2$ ,  $\rho_1$  and  $\rho_2$ .

## 5.2 Discontinuity Detection: An Algorithm

The method used to detect discontinuities (which produce mixed points at the sensor’s range output) reduces to that of estimating the value of  $S = \partial^2(V^2)/\partial A_1^2$  numerically from successive data batches, as the sensor scans the environment. The larger  $S$  is, the more likely it is that we have crossed a discontinuity. We compare the experimentally calculated value of  $S$  to a theoretical value that we predict from equation (27). We now explain how we compute a theoretical threshold for  $S$ , above which we assume we have detected a discontinuity and explain in Section 5.5 how we experimentally measure  $S$  with the sensor data.

Let us choose a value  $S = S_{th}$ , above which we assume we have detected a discontinuity between end points. If we choose a value for  $S_{th}$  to be small, the detector will be extremely sensitive to small changes in end conditions. It will not only detect discontinuities, but may also give false detection. If  $S_{th}$  is set too large, then the sensitivity of the filter will be diminished, resulting in undetected discontinuities. The best solution would be to minimize the possibility for false detection and maximize the sensitivity simultaneously thus producing limiting values for  $R_1$  and  $R_2$  beyond which detection occurs. How to optimize these parameters simultaneously is in general an ill-defined problem, since we have no information on how to combine them.

Canny describes in his work (Canny J. 86) that in order to optimize edge detection with passive vision intensity data, the signal-to-noise ratio and the localization<sup>4</sup> of the edge can be optimized simultaneously. Canny then goes on to maximize the *product* of these two criteria but does not offer any general method by which the two effects can be optimized. In our case,  $S$  is minimized when  $R_1 = R_2$  and  $\rho_1 = \rho_2$ , maximizing the detector’s sensitivity. However, this condition also maximizes the probability of false detection. Forming a product of these two criteria will therefore not work in this case.

We therefore quantify the possibility of false detection and the detector’s sensitivity in terms of both changes in range and surface reflectance, thus providing the conditions for success and failure of the detection method.

## 5.3 False Detection and Range Sensitivity

Let us first consider the properties of the detector-to-range discontinuities (edges) only. Figure 9 shows how  $S/\rho_1^2$  in equation (27) varies with  $R_2$  for different values of  $R_1$  when  $\rho_2/\rho_1 = 1$ . It can be seen that when  $R_1 = R_2$ ,  $S = 0$  as expected. We require a value for  $S = S_{th}$  beyond which the detector indicates a discontinuity. Each curve shows that as  $R_2 \rightarrow 5.0$  m (maximum sensor range),  $S$  is minimized (excluding the minimum at  $R_2 = R_1$ ) for any  $R_1$  within the sensor’s range. If the detector is to be sensitive to changes in depth, which range from any initial  $R_1$  to  $R_2 = 5.0$  m,  $S_{th}$  must be set below this minimum value (shown as the dashed lines in each graph in Figure 9).

On the other hand, in setting  $S_{th}$  toward 0 it can be seen from the curves that the ranges of  $R_2$  that will go undetected for a given  $R_1$  become extremely small, meaning that false detection may result. To satisfy both of these “conflicting” criteria, we choose  $S_{th}$  to be a function of  $R_1$ , the sensed range estimate from the first end condition, and set  $R_2$  to 5.0 m, the maximum sensor range. This means that the detector will be sensitive enough to detect all changes in  $R_1$  and  $R_2$ , that rise above the value of  $S$  which occurs when  $R_2 = 5.0$  m. The only values of  $S$

---

<sup>4</sup>the reciprocal of the distance between detected and true edges

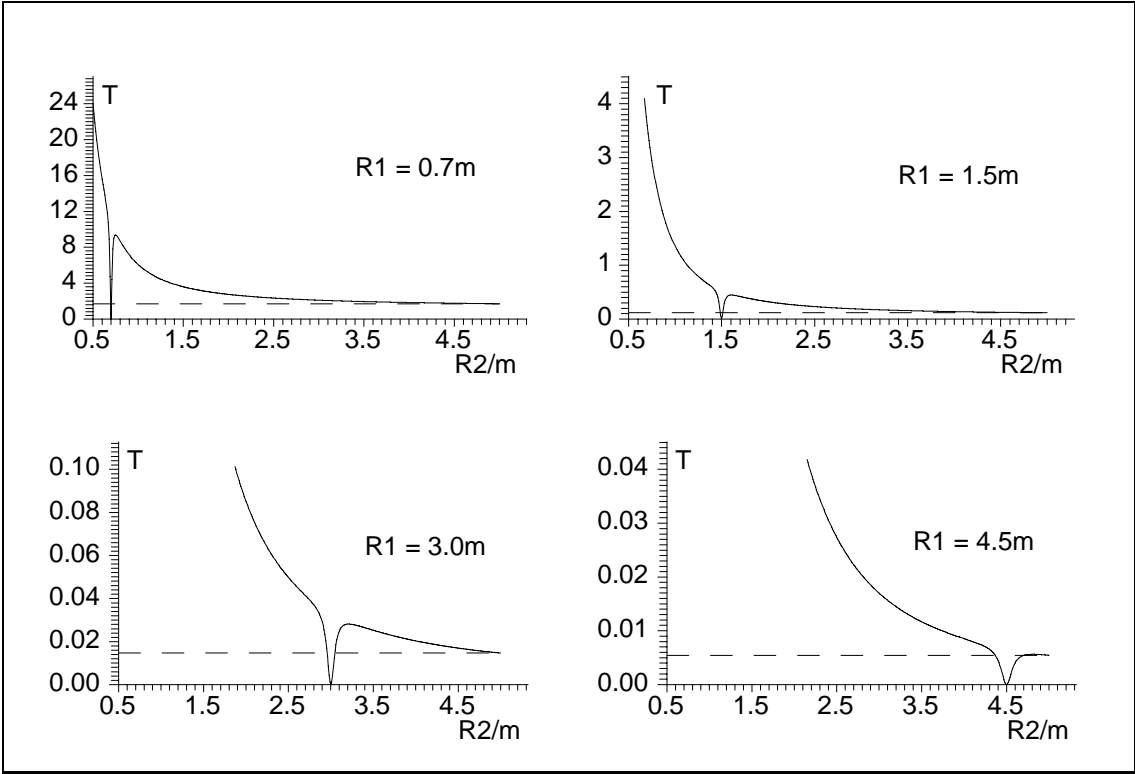


Figure 9: *Second derivative  $T = S/\rho_1^2 \times 10^3$  in equation (27) versus range  $R_2$  for various values of  $R_1$ . The dashed lines show the chosen threshold values for each value of  $R_1$ .*

that are lower than this, occur within the vicinity of  $R_2 = R_1$  below each dashed line in Figure 9.

The top left hand graph in Figure 10 shows this value of  $S_{th}$  as a function of  $R_1$ . This is obtained from equation (27) with  $\rho_2/\rho_1 = 1$  to give:

$$\frac{S_{th}}{\rho_1^2} = \frac{50 \sin^2 \gamma}{d^2 R_1^4} \left[ 1 + \left( \frac{R_1}{5} \right)^6 - 2 \left( \frac{R_1}{5} \right)^3 \cos[K(R_1 - 5)] \right] \quad (29)$$

where  $d$  is found from equation (28) with  $R_2$  set to 5.0 m. Once this value has been set, the top right hand graph in Figure 10 shows the range values of  $R_2$  that will escape detection for a given  $R_1$ . For example, at  $R_1 = 3.5$  m, provided  $3.43 < R_2 < 3.58$  m, and  $\rho_2/\rho_1 = 1$ , no detection will occur. For the value of  $S_{th}$  chosen above, the top right hand graph shows that any  $(R_1, R_2)$  coordinate that lies outside of the envelope will result in a detection, no matter what the reason. The coordinate  $R_1 = 3.5$  m and  $R_2 = 3.58$  m lies on the envelope. These values of  $R_1$  and  $R_2$  correspond to a beam-to-surface angle of incidence  $\theta$ , defined in Figure 7, of  $80^\circ$ . Objects giving a beam-to-surface angle of incidence higher than  $80^\circ$  will give false detection.

#### 5.4 Surface Reflectance Sensitivity

We now analyze the response of the detector to changes in surface reflectivity between end conditions. If  $\rho_1 \neq \rho_2$ , we have seen in Figure 5 that spurious data can also result. Under these conditions we require that  $S > S_{th}$  in order for detection. From equations (27) and (29) it can be seen that  $S > S_{th}$  only if

$$\left[ \left( \frac{\rho_2}{\rho_1} \right) - \alpha \right] \left[ \left( \frac{\rho_2}{\rho_1} \right) - \beta \right] > 0, \quad (30)$$

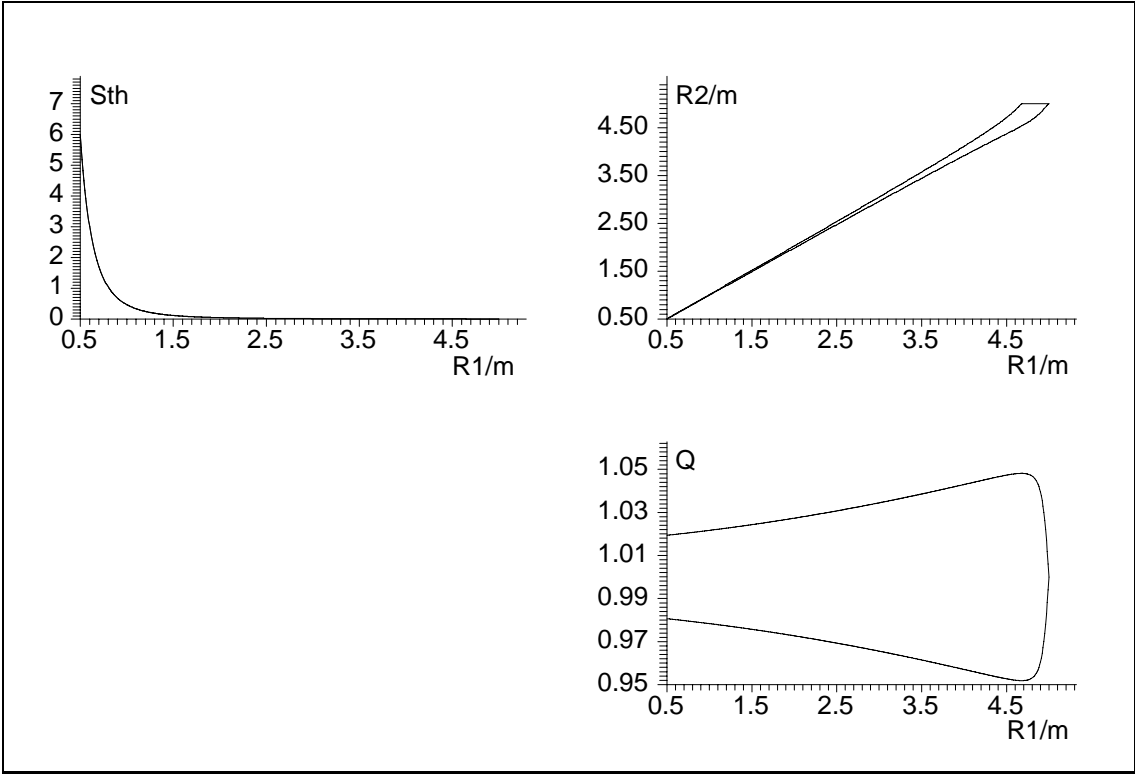


Figure 10: The top left hand graph shows the value of  $S_{th}/\rho_1^2 \times 10^3$  versus  $R_1$  that is used as a threshold beyond which a discontinuity is predicted. The top right hand graph shows an ‘envelope’ that contains pairs of values of  $R_1$  and  $R_2$  that will go undetected by the algorithm. The lower graph shows an envelope within which values of  $\rho_2/\rho_1$  will go undetected, when  $R_1 = R_2$ . The vertical axis  $Q$  represents  $\rho_2/\rho_1$  and the lines plotted are  $Q = \alpha$  and  $Q = \beta$  (see text).

where  $\alpha$  and  $\beta$  are both functions of  $R_1$  and  $R_2$  only. If  $\rho_2/\rho_1$  lies between  $\alpha$  and  $\beta$ , then detection will *not* occur.

If the threshold  $S_{th}$  were set to zero, then all values of  $\rho_2/\rho_1 \neq 1$  would be detected, since  $S$  is always greater than zero under these conditions. However, because of the false detection criterion above, the detector allows values of  $R_1$  slightly different from  $R_2$  to go undetected. As  $R_1$  and  $R_2$  begin to differ, we will see that there is interaction between range and reflectance sensitivity, since some values of  $\rho_2/\rho_1 \neq 1$  will also remain undetected. Hence, limiting the possibility of false detection degrades the sensitivity of the detector not only to range changes, but also to surface reflectance changes.

This is demonstrated in the bottom graph of Figure 10. This shows the values of  $\alpha$  and  $\beta$  in inequality (30) versus  $R_1$ , when  $R_1 = R_2$ . If  $\rho_2/\rho_1$  lies within the region shown, detection will not occur. This curve shows the sensitivity of the detector to changes in surface reflectivity *only*, since  $R_1 = R_2$ . The region is symmetrical about the line  $Q = \rho_2/\rho_1 = 1$ . For example, when  $R_1 = R_2 = 2.5$  m, surface reflectance ratios  $\rho_2/\rho_1$  between 0.97 and 1.03 will go undetected.

Finally, Figure 11 shows plots of  $\rho_2/\rho_1 = \alpha$  and  $\rho_2/\rho_1 = \beta$  when  $R_1 \neq R_2$ . The interaction between range and surface reflectance ratio is evident. If  $\rho_2/\rho_1$  lies within the regions shown, no detection occurs, even when  $R_1$  and  $R_2$  are significantly different. The larger the value of  $R_2$ , the larger the undetectable zones become.

If  $\rho_2/\rho_1 = 1$ , the detector is very sensitive to changes in range, and if  $R_1 \approx R_2$ , the detector is sensitive to changes in surface reflectivity. If both reflectance and range change simultaneously,

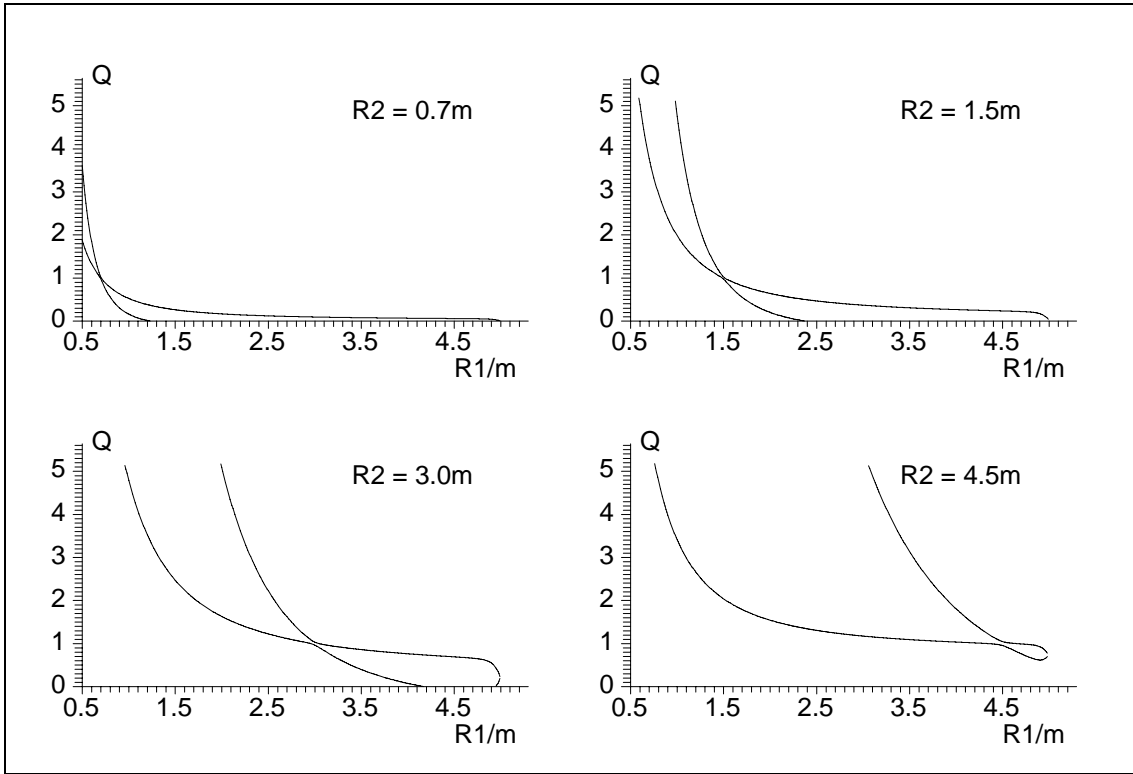


Figure 11: *Surface reflectance ratio  $Q = \rho_2/\rho_1$  versus  $R_1$  for various values of  $R_2$  as given with each graph. At certain values for  $R_1$  and  $R_2$ , if  $Q = \rho_2/\rho_1$  lies between the curves shown, no detection will occur.*

however, interaction can occur, this interaction being governed by values for  $R_1$ ,  $R_2$ , and  $\rho_2/\rho_1$  in the graphs of Figure 11. It can be seen that as the recorded range  $R_1$  is increased toward maximum range, then the area of the undetectable zone also increases (i.e. the detector becomes less sensitive to changes in surface reflectivity).

## 5.5 Practical Implementation and Results

Figure 12 shows two scans after systematic phase error correction. The left hand scan shows a dense  $360^\circ$  plot of the environment, each sample taken at a time interval of 0.1 ms. Between points J and K on the lower pillar, a colored target was positioned, causing a change in surface reflectivity. The effects of the discontinuity can be seen at J and K, and also at the pillar edges.

In this first scan we used all eight bits of the analogue-to-digital converter to convert ranges up to 2.5 m only. The scan is made up of 13,474 samples, and every 18 of these were used to form a single data point on the right hand range map. Along with each new data point, a value for  $S$  was established and compared with  $S_{th}$  in equation (29). Note that before this comparison can be done, an estimate for  $\rho_1$  is necessary in equation (29). This was estimated from a few range and signal strength pairs and the use of equation (25). The values of  $S$  at the resulting spurious points in the right hand scan of Figure 12 are very much larger than values of  $S$  caused by “normal” points.

In Figure 13 the top curve shows the variation of signal strength with angle, during the scan of Figure 12. Notice the dip at an angle of approximately  $85^\circ$  due to region JK in Figure 12. The lower graph shows the estimated value of  $S$  for each data point in the right hand plot of the scan. The large spikes occur at both range and reflectance discontinuities. Superimposed on

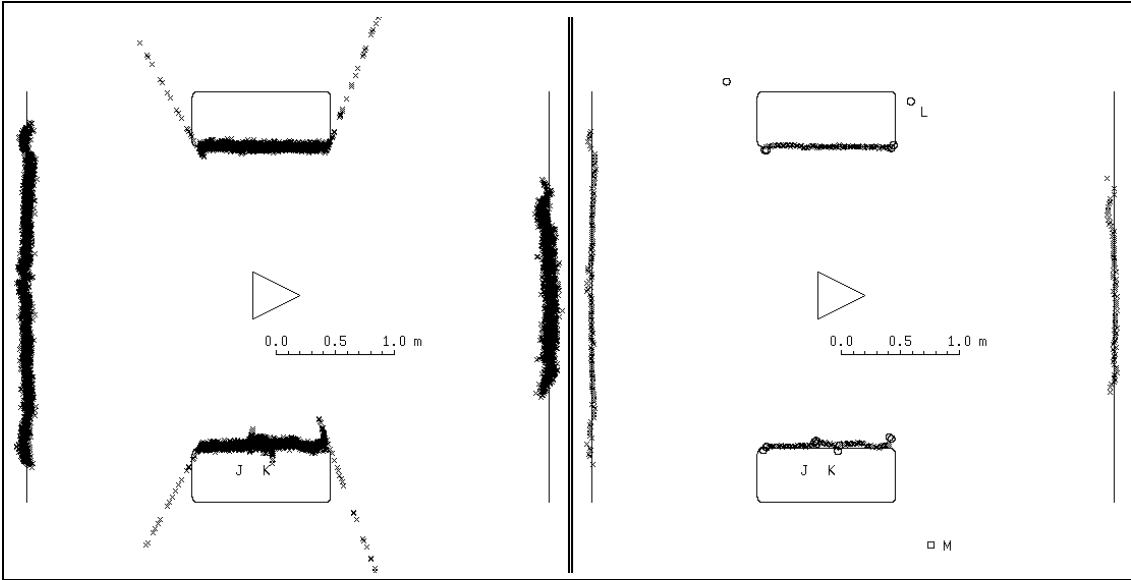


Figure 12: *Discontinuity detection using 13,474 samples from a single scan. In the right hand scan detected discontinuities are plotted as circles, and points with zero returned signal amplitude are shown as squares.*

this plot is a curve of  $S_{th}$  versus sensor angle. Notice how  $S_{th}$  adapts to the changes in range at angles of approximately  $70^\circ$ ,  $115^\circ$ ,  $240^\circ$  and  $290^\circ$ . Only the spikes produced in the estimation of  $S$  rise above  $S_{th}$ . These points are plotted as circles in the right hand scan of Figure 12, see for example point L in the figure.

We now have enough information from the sensor to be able to produce the scans shown in Figure 14. The left hand scan shows “filtered” or trustworthy data. Each data point in this scan has passed through the discontinuity detector successfully and has an associated range variance estimate. The right hand plot shows the points that failed the discontinuity test. Point M (shown as a square in Figures 12 and 14) has occurred as a result of the sensor estimating that all 18 data samples from the left hand scan of Figure 12 have a signal amplitude of 0 volts. This is an example of an undesirable feature of the particular sensor used, namely, its inability to always estimate a finite signal amplitude when the actual signal amplitude falls below a certain value. Because of this,  $S$  cannot be estimated, and we cannot place any confidence in this data point.

Hence, within the working capabilities of our discontinuity detector (outlined in Section 5.4), we are confident that all of the range data shown in the left hand scan of Figure 14 are “true” data. Notice also the much improved variance in the range data of the right hand scan of Figure 12 compared with that in the left scan due to the averaging of 18 samples per data point (Adams M. D. 92).

Figure 15 shows an uncorrected scan (left hand plot) and a systematic phase-corrected scan (right hand plot). The number of samples recorded was reduced to 5600.

Notice that the sensor is sensitive enough to resolve the small changes in the range data in Figure 15, caused by thin vertical pipes on the wall at A and B. The graphs in Figure 16 show the variation of  $S_{th}$  and  $S$  versus sensor azimuth, as the scan was recorded. Notice again that the detector adapts its thresholding technique to the environment surrounding the sensor, according to equation (29). Figure 17 shows the results of using the thresholding technique on the calibrated data from Figure 15. The left hand scan shows data that have successfully passed through the detector. The right hand scan shows the data that either carried no returned signal

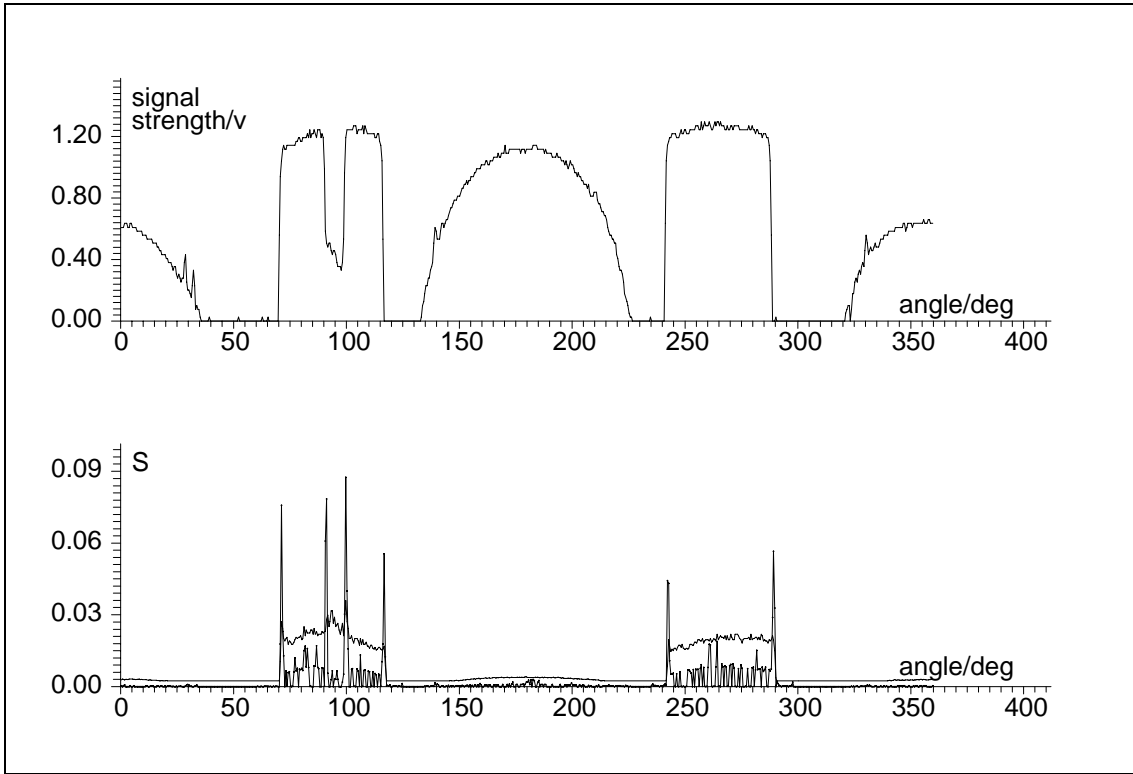


Figure 13: *Signal amplitude (top graph) and  $S$  (bottom graph) versus scan angle as computed experimentally during the previous scan.  $S_{th}$  is superimposed on the data in the lower graph.*

strength (plotted as squares) or failed the discontinuity test (plotted as circles).

This scan shows another poor quality of the particular sensor used. It is not always able to produce a nonzero signal amplitude output when reporting a range estimate. It was sometimes observed that predictable, or “reasonable” range estimates could be produced by the sensor, while the signal amplitude gave zero output. The sensor therefore incorrectly informed us that we had no confidence in the range estimate. This occurs at point M in Figure 17. Clearly the data produced here and farther up the wall are not random, yet because the sensor’s signal amplitude output gives zero volts, no values for  $S$  or  $\langle \sigma_r^2 \rangle$  can be correctly assigned to these points.

Therefore, a useful design criterion for such a sensor is that it should output a finite signal amplitude for any predictable range estimate. The above model could then be used with as much received data as possible. (Nitzan D. et al. 77), (Hebert M. and Krotkov E. 91) and (Miller G. L. and Wagner E. R. 87) report in their work that the received signal strength has a very large dynamic range of optical intensity. This can span several thousands to one. In response to this problem, Nitzan et al. measured the received signal amplitude with a logarithmic amplifier (Nitzan D. et al. 77). Signal amplitude outputs that are extremely small can then be reproduced faithfully.

Points P and Q in Figure 17 show data resulting from a split optical beam at the edge of the pillar close to the mobile. At point P, not enough of the pillar is illuminated to give any signal amplitude estimate. The discontinuity detector cannot operate here, and therefore a square is plotted at P. At Q, however, enough of the optical beam illuminates the pillar so that the net signal amplitude with each of the four points used to create point Q can be used to estimate  $S$ . Q has been captured by the discontinuity detector.

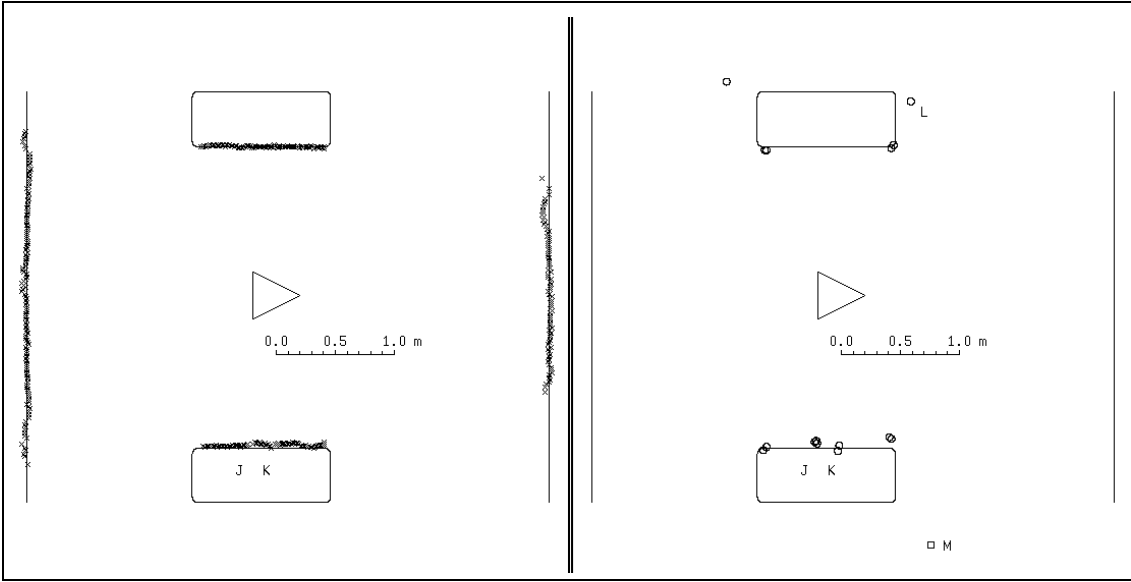


Figure 14: Range data that has successfully passed through the discontinuity detector (left scan) and data that has failed the test (right scan). The raw data is shown in Figure 12

Points R and S in the left hand plot in Figure 17 have escaped detection, resulting from a combination of  $R_1$ ,  $R_2$  and  $\rho_2/\rho_1$  that falls within one of the undetectable zones in Figure 11.

## 6 Summary

In this article we have presented a model for an AMCW optical range finder and demonstrated a two-dimensional edge-detecting algorithm. Gaining an understanding of both the amplitude and range data is essential if the sensor is to be used at its best.

In particular we have examined the following issues:

1. For most returned signal amplitudes, we know that the sensor's output range distribution is approximately Gaussian and that the range variance of a single sample can be determined from the signal amplitude, according to equation (8).
2. Previous work has acknowledged the existence of "spurious" or "phantom" data points, as shown in Section 5, (Hebert M. and Krotkov E. 91). We have considered in detail the effect of splitting the light beam between two targets. In previous work the cause of the spurious points has not received much attention, and it has simply been stated that they are inherent in any AMCW optical system and cannot be removed (Hebert M. and Krotkov E. 91).

In response to this we have built a detector that has a high success rate at identifying such points when they are caused by *either* reflectance *or* range changes. When both effects occur simultaneously, we have quantified the interaction which, under certain circumstances, can result in no detection. The detector is not fool-proof, and we have indeed shown that the sensitivity of the detector decreases with increasing range. An interesting possibility for future research could be to select a different adaptive threshold function to that used here, so that within the ranges of interest, the filter could be as sensitive as possible.

It is worth noting that decreasing the cross-sectional area of the optical beam or simply

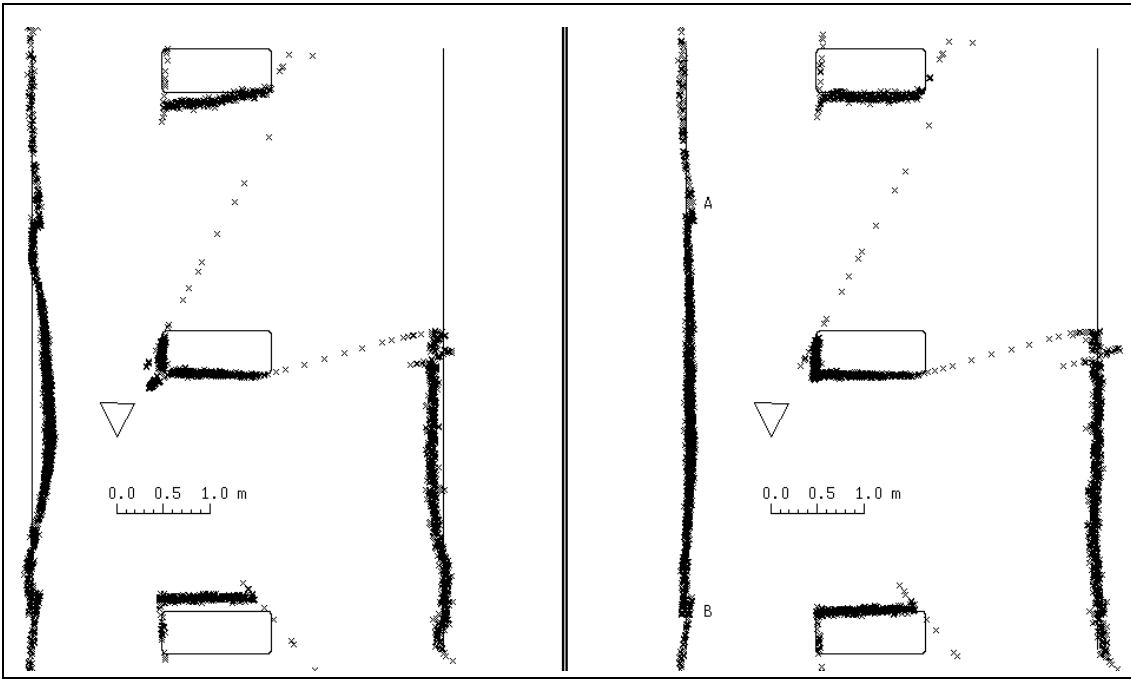


Figure 15: *Uncorrected (left) and corrected (right) range scans using 5600 data samples.*

using a laser can reduce the amount of spurious points recorded per scan, but it cannot altogether eliminate them.

3. In the robotics field, the ultimate test of any algorithm must be in its application. We have used the discontinuity detector and sensor model presented above, together with a simple navigational algorithm to guide a small mobile platform using the AMCW sensor in a cluttered indoor scene (Adams M. D. 92). The algorithms have worked consistently over a wide variety of configurations.

## 7 Acknowledgments

This work was supported by the Science and Engineering Research Council (including the Application of Computers to Manufacturing Engineering Directorate). We thank other members of the Robotics Research Group in Oxford for their support and encouragement.

## References

- Adams M. D., 1992. *Optical Range Data Analysis for Stable Target Pursuit in Mobile Robotics*. PhD thesis, University of Oxford, United Kingdom.
- Besl P. J., 1988. *Surfaces in Range Image Understanding*. New York: Springer-Verlag.
- Canny J., 1986 (November). A computational approach to edge detection. In *IEEE Trans. Pattern Analysis Machine Intell.*, pages 679–697, vol. 8.
- Connor F. R., 1982. *Noise*. London: Edward Arnold.
- Cox I. J., 1988. Blanche: An autonomous robot vehicle for structured environments. In *Proc. IEEE Int. Conf. Robotics and Automation*, pages 978–982.

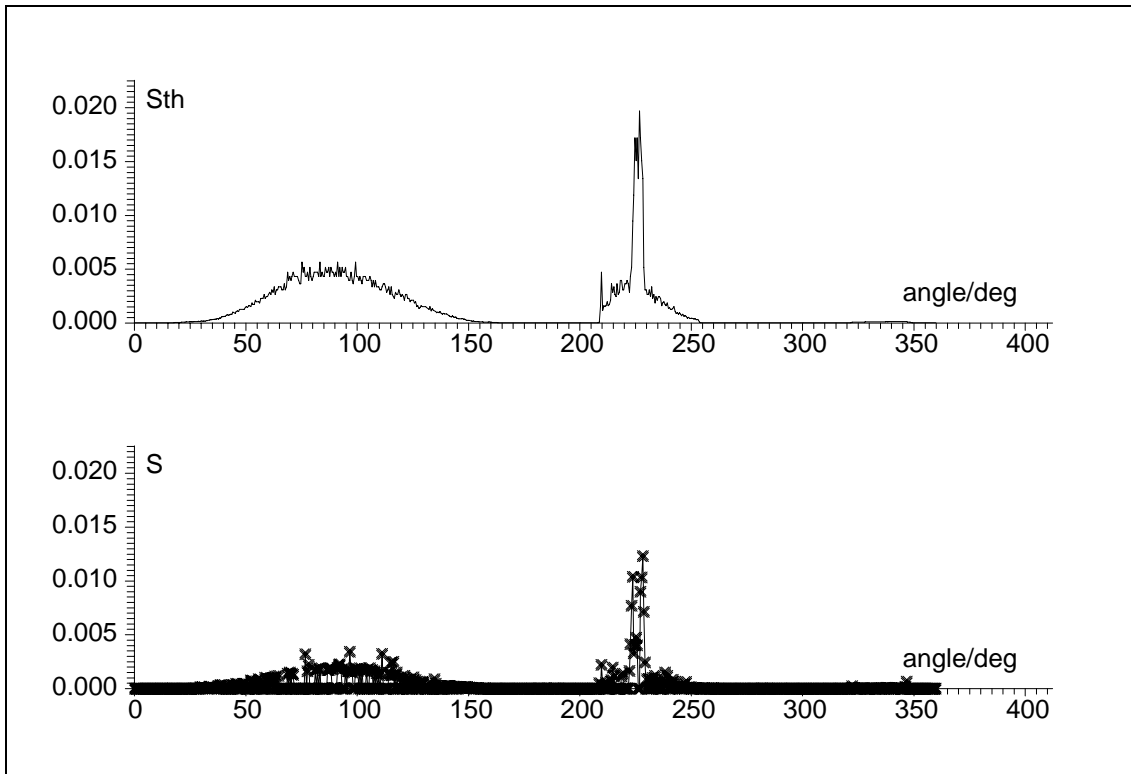


Figure 16:  $S_{th}$  (top graph) and  $S$  (bottom graph) versus sensor azimuth for the calibrated scan in the previous figure.

Hebert M. and Krotkov E., 1991. 3-D measurements from imaging laser radars: How good are they? In *Int. Conf. Intelligent Robots and Systems*, pages 359–364.

Hebert M., Krotkov E., and Kanade T., 1989. A perception system for a planetary explorer. In *International Conference on Decision and Control*, pages 1151–1156.

Hinkel R. and Weidmann M., 1989. *First Results in Real Time Position Estimation with a Laser Radar*. Technical Report, Computer Science Department, University of Kaiserslautern, Germany.

Johnston A. R., 1973. *Infra-red Laser Rangefinder*. Technical Report, Jet Propulsion Laboratory, Pasadena, CA.

Krotkov E., 1990. *Laser Rangefinder Calibration for a Walking Robot*. Technical Report, Robotics Institute, Carnegie Mellon University, Pittsburgh PA.

Miller G. L. and Wagner E. R., 1987. *An Optical Rangefinder for Autonomous Robot Cart Navigation*. Technical Report, A.T&T. Bell Laboratories, Princeton NJ.

Moon P., 1961. *The Scientific Basis of Illuminating Engineering*. New York: Dover Publications.

Nitzan D., Brain A. E., and Duda R. O., 1977. The measurement and use of registered reflectance data in scene analysis. In *Proc. IEEE.*, pages 206–220, vol. 65.

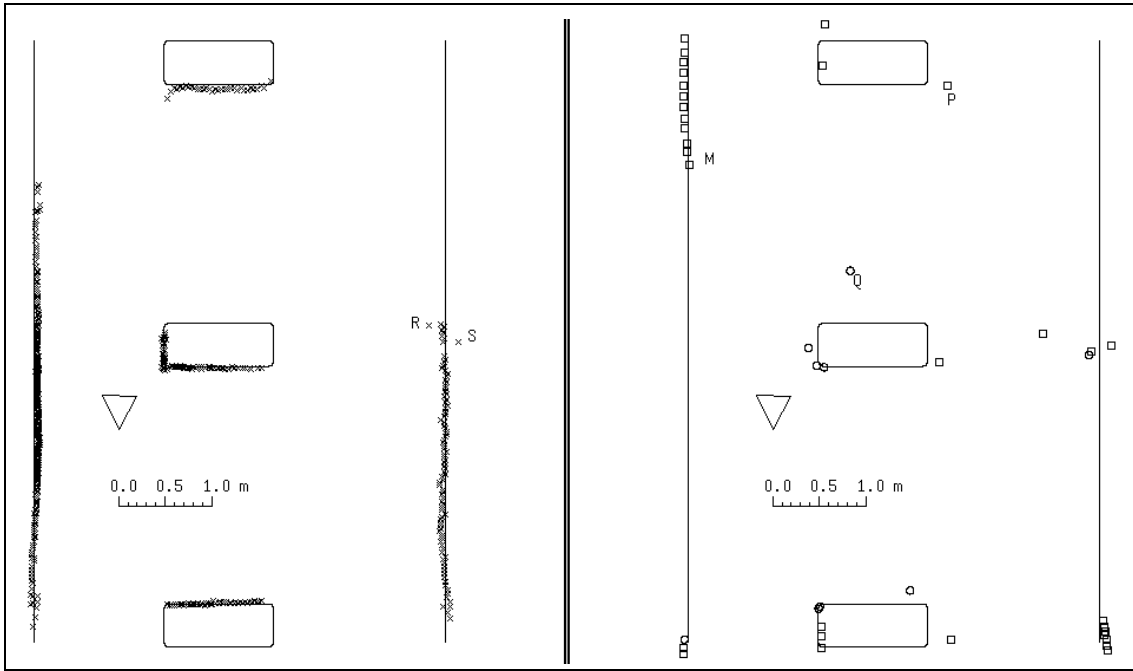


Figure 17: Accepted (left) and rejected (right) data, after filtering with the detector